Journal of
Applied Physics

RESEARCH ARTICLE | DECEMBER 11 2024

Effect of physical vapor deposition on contacts to 2D MoS_2

M. Saifur Rahman ; Ama D. Agyapong ; Suzanne E. Mohney

Check for updates

J. Appl. Phys. 136, 224303 (2024)
https://doi.org/10.1063/5.0231261

View
Online

Export
Citation

Articles You May Be Interested In

Electrostatic properties of few-layer MoS_2 films

AIP Advances (April 2013)

Two-dimensional charge carrier distribution in MoS_2 monolayer and multilayers

Appl. Phys. Lett. (March 2019)

Synthesized multiwall MoS_2 nanotube and nanoribbon field-effect transistors

Appl. Phys. Lett. (January 2015)

10 February 2025 18:26:00

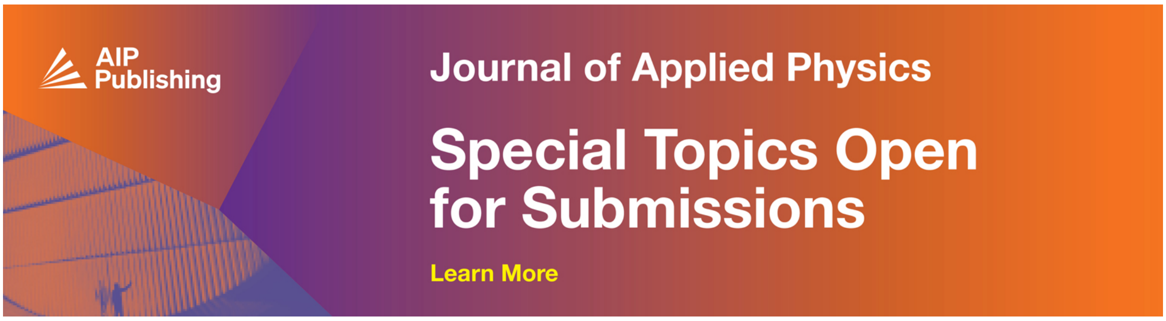
AIP Publishing
Journal of Applied Physics
Special Topics Open for Submissions
Learn More

AIP Publishing

Journal of Applied Physics ARTICLE pubs.aip.org/aip/jap

Effect of physical vapor deposition on contacts to 2D MoS_2

Cite as: J. Appl. Phys. **136**, 224303 (2024); doi: 10.1063/5.0231261
Submitted: 29 July 2024 · Accepted: 19 November 2024 ·
Published Online: 11 December 2024

M. Saifur Rahman,[1,a)] Ama D. Agyapong,[2] and Suzanne E. Mohney[1,2]

AFFILIATIONS

[1]Department of Electrical Engineering, Penn State University, University Park, Pennsylvania 16802, USA
[2]Department of Materials Science and Engineering, Penn State University, University Park, Pennsylvania 16802, USA

[a)]**Author to whom correspondence should be addressed:** mohney@psu.edu

ABSTRACT

Two-dimensional (2D) molybdenum disulfide (MoS_2) holds immense promise for next-generation electronic applications. However, the role of contact deposition at the metal/semiconductor interface remains a critical factor influencing device performance. This study investigates the impact of different metal deposition techniques, specifically electron-beam evaporation and sputtering, for depositing Cu, Pd, Bi, Sn, Pt, and In. Utilizing Raman spectroscopy with backside illumination, we observe changes at the buried metal/1L MoS_2 interface after metal deposition. Sputter deposition causes more damage to monolayer MoS_2 than electron-beam evaporation, as indicated by partial or complete disappearance of first-order $E'(\Gamma)^\alpha$ and $A'_1(\Gamma)^\alpha$ Raman modes post-deposition. We correlated the degree of damage from sputtered atoms to the cohesive energies of the sputtered material. Through fabrication and testing of field-effect transistors, we demonstrate that electron-beam evaporated Sn/Au contacts exhibit superior performance including reduced contact resistance (~12×), enhanced mobility (~4.3×), and lower subthreshold slope (~0.6×) compared to their sputtered counterparts. Our findings underscore the importance of contact fabrication methods for optimizing the performance of 2D MoS_2 devices and the value of Raman spectroscopy with backside illumination for gaining insight into contact performance.

10 February 2025 18:26:00

© 2024 Author(s). All article content, except where otherwise noted, is licensed under a Creative Commons Attribution (CC BY) license (https://creativecommons.org/licenses/by/4.0/). https://doi.org/10.1063/5.0231261

I. INTRODUCTION

The two-dimensional (2D) transition metal dichalcogenide (TMD) molybdenum disulfide (MoS_2) is a desirable channel material for field-effect transistors (FETs) due to its structural and semiconducting properties for devices approaching the sub-nanometer scale.[1,2] Molybdenum disulfide has strong covalent bonds within its layers and weak van der Waals bonds between its layers, which can be cleanly broken to produce a single layer of MoS_2. Monolayer MoS_2 provides an atomically flat and potentially dangling-bond-free van der Waals surface and a bandgap of 1.8 eV for high-performance FETs.[3,4] However, high contact resistance (RC)at the metal/semiconductor interface impedes FET performance.[3,5] In addition, interfacial reactions between contact metals and 1L MoS_2 could lead to high contact resistance in MoS_2-based FETs.[6]

Preparing atomically sharp and clean metal/semiconductor interfaces can help overcome the Fermi-level pinning effect in 2D semiconductor devices,[7–9] allowing engineers to tailor the Schottky barrier height and reduce contact resistance. Sputtering allows for the deposition of alloys and compounds with precise control over composition, making it easier to achieve the desired stoichiometry from a single source.[10,11] The ability to deposit alloys and compounds is particularly valuable when forming contacts to 2D materials, making it possible to tailor the work function[12,13] or topological properties[14] or superconductivity[15] of a contact metallization. However, metallization processes can introduce crystal lattice disorder near the metal/2D material interface and result in Fermi-level pinning.[8,16,17] Despite the higher energy of sputtered atoms (typically 2–7 vs ~0.1 eV for evaporated atoms),[18] the approach has been of interest in the literature. Radio frequency (RF) sputtering of Sb_2Te_3[19] has been used to prepare van der Waals (vdW) contacts to MoS_2, offering high thermal stability and low contact resistance. The improved performance is attributed to Fermi-level unpinning, a small band offset between Sb_2Te_3 and MoS_2, and a low density of states in Sb_2Te_3, leading to better results in MoS_2 MOSFETs with Sb_2Te_3/W contacts compared to Sb/W contacts.

Thermal and electron-beam evaporation are often used for contact deposition on MoS_2, but they come with additional concerns such as the need for precise control over the deposition rate and chamber pressure. These factors can impact the performance of contacts, potentially leading to a variation in device characteristics and reliability. For example, Wang *et al.* showed that when the deposition rate of Au by electron-beam evaporation is high, the performance of FETs was degraded, possibly due to radiative heating.[20] Other recent research on 2D memristors reveals that high Au electron-beam evaporation rates can cause local damage to MoS_2, with Au atoms penetrating the layers, impacting memristor performance. Their study found reliability improvements with low Au deposition rates and thicker MoS_2, as higher rates negatively affected memristor performance by inducing localized disorder at the contact inferface.[21] To minimize radiation damage from x-ray exposure during e-beam evaporation, Wang *et al.*[22] recommend intermittent deposition at a relatively high rate (as reported earlier by Wang *et al.*[20]) to reduce x-ray exposure, with pauses to stabilize pressure between steps. Another study reports that Au electron-beam evaporated in ultrahigh vacuum ($\sim 10^{-9}$ Torr) offers three times lower contact resistance compared to ordinary conditions ($\sim 10^{-6}$ Torr),[23] while others claim that a moderate vacuum of 5×10^{-6} Torr still permits the formation of a high-quality[24] quasi-van der Waals interface. Yet other studies have examined the effect of deposition pressure, revealing the potential for oxide formation at the contact interface (for Ni[25] or Ti[26]) if the base pressure is not sufficiently low, although Bi contacts[25] showed no significant difference in contact resistance or interfacial chemistry between ultrahigh vacuum and high vacuum conditions. High reactivity of metal atoms involved in the deposition process can also greatly alter or even destroy a monolayer MoS_2 film.[27,28] It is, therefore, important to investigate metal deposition to understand better and control electronic transport in nanoscale MoS_2 devices.

In this work, we investigate the deposition of different metals on MoS_2 using two physical vapor deposition techniques for each and study the impact of metallization on the vibrational and electronic properties of MoS_2. We find that sputter deposition causes more damage to monolayer MoS_2 than electron-beam evaporation, as evidenced by greater suppression of first-order Raman modes, and we correlate this damage with the cohesive energies of the metals. Furthermore, we compare the performance of field-effect transistors fabricated with e-beam evaporated and sputtered Sn/Au contacts. We selected Sn/Au contacts because low-melting-point metals such as Bi,[29] Sn,[30] and In[30] have been reported to offer low contact resistance on 1L MoS_2 in recent studies without damage to 1L MoS_2.[29,30] Among these metals, Sn was chosen to explore differences in contact resistance, with Au added as a capping layer for ease of probing.

II. EXPERIMENTAL APPROACH

A. Thin film deposition

Monolayer MoS_2, synthesized by metalorganic chemical vapor deposition (MOCVD) on 2 in. sapphire substrates as previously described,[31,32] were obtained from the 2D Crystal Consortium (2DCC) at Pennsylvania State University and cleaved into smaller pieces for sample fabrication. Metal thin films were deposited directly onto the 1L MoS_2 by electron-beam evaporation or DC magnetron sputtering to determine the effects of each physical vapor deposition technique on MoS_2. We compared electron-beam evaporated Bi, Cu, In, Pd, Pt, and Sn films to their sputtered counterparts. These metals have been used previously in reported contacts to MoS_2.[4,29,33–35] All electron-beam evaporation occurred in a chamber with base pressure $<5 \times 10^{-7}$ Torr, and the chamber was gettered prior to electron beam evaporating the metals of interest by depositing 30 nm of Ti with the sample shutter closed to remove background reactive species (such as H_2O vapor) in the deposition system. More details on the conditions for the electron-beam evaporation of each metal are found in Table S1.1 in the supplementary material 1). Details about the conditions for the sputter deposition of each metal are also provided in Table S1.2 in supplementary material 1. The metal films were nominally 100 nm thick except for electron beam evaporated Pt (70 nm), which was intentionally made thinner to mitigate the heat generated during its evaporation. Samples remained in the vacuum chamber or were vacuum sealed or stored in a nitrogen dry box until it was time to collect Raman spectra to reduce possible effects from the ambient environment.

B. Raman spectroscopy

Raman spectroscopy is a fast and non-destructive technique previously used to study doping, strain, and damage in 1L MoS_2[36] and 1L MoS_2 top-gated FETs.[37] Studies that used Raman spectroscopy to observe the effects of metal contacts on TMDs were limited to studying ultra-thin (<2 nm) metal films due to the restriction of maintaining metal transparency.[6] We need an alternative approach to understand the buried metal/MoS_2 interface in a FET structure, since ultra-thin contact metals could result in discontinuous films.[27] We have already established a backside-illumination Raman spectroscopy technique and demonstrated its use in probing various metal/1LWS_2 interfaces to observe interfacial reactions.[28] In this study, we applied the backside-illumination method to subsequent experiments in this paper to study the effects of electron beam evaporated and sputtered metal thin films on 1L MoS_2.

We collected numerous Raman spectra from various areas of the metal/1LMoS_2/sapphire samples using a LabRAM HR Evolution (Horiba Scientific Co.) spectrometer with ultra-low-frequency (ULF) 532 nm laser excitation at a power of 1.7 mW (5% of 34 mW @ 100%). We collected each scan twice using a grating with 1800 lines/mm and a near infrared 50× objective lens over a spectrum range from -150 to 800 cm^{-1} for 30 s. The 532 nm laser was focused through the transparent sapphire substrate (backside illumination) using a backscattering geometry (Fig. 1). The backscattering geometry coupled with the backside illumination allows us to probe a buried metal/TMD interface and non-destructively detect an underlying TMD monolayer, if still present, after metallization.[28] We did not observe any differences in the Raman spectra for 1L MoS_2 between the data collected with the topside illumination backscattering geometry and data collected via the backside-illumination backscattering geometry, as described in more detail in Fig. S2.1 in supplementary material 2. The Raman spectra were plotted using the LabSpec 6 Imaging and Spectroscopy Software (Horiba Scientific Co.) and normalized to the sapphire peak. Spectra were fitted with the Gaussian–Lorentzian fit to determine the peak positions and full width at half maxima (FWHM). Further information

10 February 2025 18:26:00

© Author(s) 2024

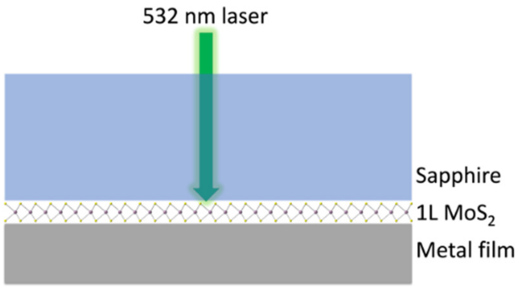

FIG. 1 Illustration of the backscattering geometry configuration coupled with the backside-illumination method for Raman data acquisition.

is provided in supplementary material 3, which provides more information about the process and shows the fit for each metal. However, we report FWHM only for spectra with low signal-to-noise ratios. The peak positions and corresponding FWHM were averaged over all acquired spectra for each sample with a standard deviation of ≤0.7 cm^{-1} for the peak position and ≤1.1 cm^{-1} for the FWHM.

C. Device fabrication and measurement

To fabricate the devices, the MoS$_2$ monolayer was transferred onto Al$_2$O$_3$/Pt/TiN/*p* + Si via poly (methyl methacrylate) (PMMA)-assisted wet-transfer.[38] To define the channel regions of the MoS$_2$ FETs in this study, substrates with transferred MoS$_2$ were spin-coated with PMMA A6 at 4000 RPM for 45 s and then baked at 180 °C for 180 s. The resist was exposed using electron beam (e-beam) lithography and developed with a 1:1 mixture of 4-methyl-2-pentanone (MIBK) and isopropyl alcohol (IPA) for 80 and 40 s, respectively. The exposed monolayer MoS$_2$ was etched using an SF$_6$ and O$_2$ plasma at 5 °C for 25 s. Following this, the samples were rinsed in acetone and IPA to remove the e-beam resist. For defining the source and drain contacts, a bilayer resists of A3 PMMA and A6 PMMA was spin-coated onto the samples. E-beam lithography was used again to define these contacts, with development performed using the same MIBK and IPA mixture. Metal contacts were deposited using e-beam evaporation or sputter deposition (30/20 nm Sn/Au). Finally, the samples underwent a lift-off process to remove excess resist and metal by immersing in acetone for 1 h, followed by IPA for an additional 30 min. Measurements were performed using a semi-automated Formfactor 12 000 probe station under atmospheric conditions with a Keysight B1500A parameter analyzer.

III. RESULTS AND DISCUSSION

A. Effects of deposited metals on the Raman spectra of MoS$_2$

1. Identified peaks and positions

A reference Raman spectrum was collected for bare 1L MoS$_2$ using the backside-illumination method as the baseline for analysis, and it provides the same peak positions as for topside illumination (confirmation is provided in supplementary material 2 where deconvoluted spectra are compared). Peak positions for bare and metallized 1L MoS$_2$ are listed in Table I. In Fig. 2, this same spectrum for bare MoS$_2$ is shown as the top figure in each part along with spectra collected after electron-beam evaporation and sputter deposition of each metal, with the metals Cu, Pd, Pt, Bi, Sn, and In shown in Figs. 2(a)–2(f), respectively. Peak deconvolution is shown for each metallized sample in the figures in supplementary material 3. We detected the first-order in-plane and out-of-plane Raman modes for 1L MoS$_2$, $E'(\Gamma)^{\alpha}$ at 386.1 cm^{-1} and $A'_1(\Gamma)^{\alpha}$ at 405.3 cm^{-1}, respectively.[36,39] The broad shoulder on the low-frequency side of the $E'(\Gamma)^{\alpha}$ peak is a convolution of the $E'(M)^{LO_2}$ mode referenced

10 February 2025 18:26:00

TABLE I. Peak positions for bare 1L MoS$_2$ and 1L MoS$_2$ under metals (Cu, Pd, Pt, Bi, Sn, and In) deposited by electron-beam evaporation and sputtering on 1L MoS$_2$. Peak positions are in cm^{-1}.

Material	$E'(M)^{LO_2}$	$E'(\Gamma)^{\alpha}$	Low $A'_1(\Gamma)^{\alpha}$	High $A'_1(\Gamma)^{\alpha}$	2LA (M)	$E''(M)^{TO_1}$ − ZA (M)
MoS$_2$	377.4	386.1	…	405.3	456.2	464.2
			Evaporated metals			
Cu	373.6	384.1	…	404.5	…	…
Pd	…	384.0	…	405.6	…	…
Pt	…	384.6	…	405.6	…	…
Bi	…	383.8	399.3	405.1	…	…
Sn	…	384.4	397.3	406.0	457.2	465.1
In	…	384.6	393.7	405.5	456.2	465.2
			Sputtered metals			
Cu	374.3	384.3	…	404.6	…	…
Pd	…	384.5	…	404.7	…	…
Pt	…	…	…	…	…	…
Bi	…	384.5	400.2	406.2	…	…
Sn	377.6	384.0	399.5	404.7	…	…
In	…	…	…	…	…	…

© Author(s) 2024

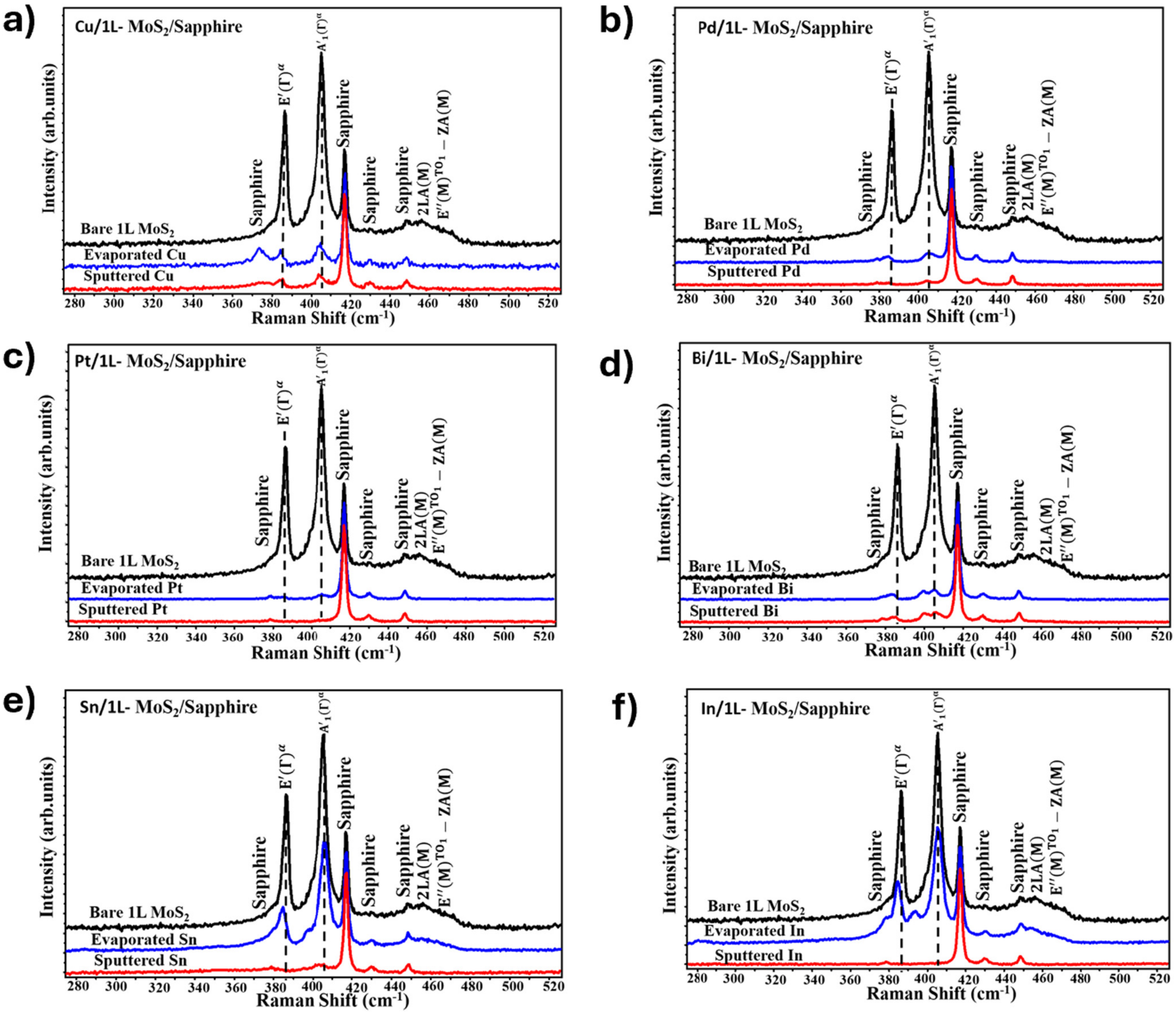

FIG. 2 Raman spectra of bare 1L MoS_2 and metalized 1L MoS_2 with evaporated and sputtered films. (a) Cu, (b) Pd, (c) Pt, (d) Bi, (e) Sn, (f) In. The first-order MoS_2 Raman modes are labeled for reference in the MoS_2 spectrum. Sapphire peaks originate from the substrate.

at $377.4\,\text{cm}^{-1}$ for 1L MoS_2[36] and a sapphire peak at $379\,\text{cm}^{-1}$. We assigned the 2LA(M) acoustic phonon and the $E''(M)^{TO_1} - ZA(M)$ multiphonon modes to the broad peak from ~455to $467\,\text{cm}^{-1}$.[40] Peaks originating from the sapphire substrate are located at 379, 417, 430, and $448\,\text{cm}^{-1}$.[41] The metalized 1L MoS_2 Raman spectra are presented in Fig. 2 for Cu, Pd, Pt, Bi, Sn, and In, respectively.

The first-order $E'(\Gamma)^{\alpha}$ and $A'_1(\Gamma)^{\alpha}$ 1L MoS_2 Raman modes remained for all electron-beam evaporated metals [Figs. 2(a)–2(f)], although they are weak after the deposition of Pd and very weak after the deposition of Pt. The $E'(\Gamma)^{\alpha}$ mode for MoS_2 beneath Cu, Pd, Pt, Bi, Sn, and In is located at 384.1, 384.0, 384.6, 383.8, 384.4, and $384.6\,\text{cm}^{-1}$, respectively. All evaporated metals exhibited a red shift of approximately $2\,\text{cm}^{-1}$ in the $E'(\Gamma)^{\alpha}$ mode. The $A'_1(\Gamma)^{\alpha}$ modes for evaporated Cu, Pd, Pt, Bi, Sn, and In samples are located at 404.5, 405.6, 405.6, 405.1, 406.0, and $405.5\,\text{cm}^{-1}$, respectively [Figs. 2(a)–2(f)]. Evaporated Pd, Pt, Sn, and In samples exhibited a blue shift of $<1\,\text{cm}^{-1}$ [Figs. 2(b), 2(c), 2(e) and 2(f)], but Cu and Bi samples exhibited a red shift of $<1\,\text{cm}^{-1}$ in the $A'_1(\Gamma)^{\alpha}$ mode [Figs. 2(a) and 2(d)]. The shifts of the $A'_1(\Gamma)^{\alpha}$ modes are within the spectral resolution of the Raman data.

An additional peak, which we identified as the $E'(M)^{LO_2}$ mode, remains after depositing Cu with a peak position of $373.6\,\text{cm}^{-1}$ after

10 February 2025 18:26:00

© Author(s) 2024

evaporation and 375.1 cm^{-1} after sputtering, although much broader, resulting in red shift of ~4 and ~2 cm^{-1} compared with bare 1L MoS_2 [Fig. 2(a)]. This peak does not show up for the other metals deposited [Figs. 2(b)–2(f)]. We do not know why we observe the $E'(M)^{LO_2}$ mode in some cases but not others. Although Cu_2S, Cu_9S_5, Cu_9S_8, or CuS could contribute peaks near 470 +/− or 261 +/−5 cm^{-1}, there are no peaks expected from copper sulfides from 373 to 375 cm^{-1}.[42] Using polarized light could have helped us further confirm the identification, but we did not take this step.

The first-order $E'(\Gamma)^\alpha$ and $A'_1(\Gamma)^\alpha$ 1L MoS_2 Raman modes remained after sputtering Cu, Pd, Bi, and Sn [Figs. 2(a), 2(b), 2(d), and 2(e)], but disappeared after sputtering Pt and In [Figs. 2(c) and 2(f)]. The $E'(\Gamma)^\alpha$ mode for Cu, Pd, Bi, and Sn is located at 384.3, 384.5, 384.5, and 384.0 cm^{-1}, respectively, and exhibited a red shift of approximately 2 cm^{-1}. The $A'_1(\Gamma)^\alpha$ mode for Cu, Pd, Bi, and Sn is located at 404.6, 404.7, 406.2, and 404.7, respectively [Figs. 2(a), 2(b), 2(d) and 2(e)]. These shifts in the $A'_1(\Gamma)^\alpha$ mode for the sputtered metals were <1 cm^{-1} and within the spectral resolution of the Raman data.

According to the literature, red shifts observed in the $E'(\Gamma)^\alpha$ modes could be due to strain or structural effects,[43] and shifts observed in the $A'_1(\Gamma)^\alpha$ modes can be due to doping or electronic effects.[36] The $A'_1(\Gamma)^\alpha$ mode has been shown to be sensitive to doping,[44] shifting to lower frequencies (red shift) when the MoS_2 undergoes *n*-type doping[45] and higher frequencies (blue shift) when it undergoes *p*-type doping.[46] Shifts in the $A'_1(\Gamma)^\alpha$ mode can be associated with electron doping due to the strong electron–phonon coupling observed for the out-of-plane vibrational mode.[36] Structural disorder could lead to the appearance of new defect-induced peaks such as the LA(M) mode referenced to be around 226 cm^{-1},[47] but we did not find this peak.

The disappearance of first-order Raman modes of TMDs has been observed in cases where the monolayer TMD was consumed in a reaction.[28] Table I shows that the first-order 1L MoS_2 Raman mode after sputtering is missing for some metals, as discussed in more detail below, leading us to conclude that sputtering may induce significant damage to the 1L MoS_2.

2. Peak intensity and broadening

We observed a decrease in the intensity of the first-order 1L MoS_2 Raman modes after metal deposition. The decrease in the intensity for the $E'(\Gamma)^\alpha$ and $A'_1(\Gamma)^\alpha$ modes was severe for sputtered Pd, Pt, Sn, and In films [Figs. 2(b), 2(c), 2(e) and 2(f)], resulting in our inability to detect the first-order MoS_2 Raman modes for sputtered In [Fig. 2(f)], nor were we able to detect the $E'(\Gamma)^\alpha$ mode for sputtered Pd, Pt, and Sn films [Figs. 2(b), 2(c) and 2(e)]. We detected only a weak remnant of the $A'_1(\Gamma)^\alpha$ mode in the spectra from the sputtered Pd, Pt, and Sn samples [Figs. 2(b), 2(c), and 2(e)], which shows up as a very weak bump around the location of the referenced $A'_1(\Gamma)^\alpha$ mode. Although the peak intensity decreased for sputtered Cu and Bi, we were able to detect the first-order MoS_2 Raman modes [Figs. 2(a) and 2(d)].

The peak intensities of first-order Raman modes for various electron-beam evaporated metals are summarized in Table II as high intensity for Sn and In, medium intensity for Cu and Bi, low intensity for Pd, and very low intensity for Pt. We were still able to detect the first-order 1L MoS_2 Raman modes for all evaporated films, suggesting that evaporation is less destructive to the 1L MoS_2 than sputtering. Decreasing intensity has been observed in first-order Raman modes after evaporating very thin layers of Ag, Al, Au, and Ni onto monolayer MoS_2[48] and Au on multilayer MoS_2.[49]

Peak broadening has been associated with a decrease in the MoS_2 grain size due to phonon confinement at grain boundaries. Peak broadening can be determined by measuring the FWHM of the first-order 1L MoS_2 Raman modes and comparing it to metallized 1L MoS_2. The FWHM of the $E'(\Gamma)^\alpha$ and $A'_1(\Gamma)^\alpha$ modes for the bare 1L MoS_2 was measured to be 4.4 and 5.6 cm^{-1}, respectively. We measured the FWHM of the $E'(\Gamma)^\alpha$ and $A'_1(\Gamma)^\alpha$ modes for the evaporated samples (Table II). (We do not provide FWHM from the sputtered samples because of lower intensity or disappearance of first-order Raman modes.) The $E'(\Gamma)^\alpha$ peak narrowed by approximately 0.4 cm^{-1} after evaporating some metals (Cu, Pd, and In) remained unchanged for Pt, and increased by 1.1 and 0.3 cm^{-1} after depositing Bi and Sn, respectively. The $A'_1(\Gamma)^\alpha$ peak narrowed by 0.6–0.9 cm^{-1} for Cu, Pd, Pt, and Bi, but it increased by ~0.4 cm^{-1} for Sn and In. These changes to the FWHM are too small to conclude that the deposition of the evaporated metal films influenced the peak broadness in the underlying MoS_2 monolayer. It should be noted that the samples with evaporated metals, except for Sn and In, exhibited very low signal-to-noise ratios, making it hard to determine the FWHM with confidence. Although broadening of first-order Raman modes for 1L MoS_2 has been reported to be associated with an increase in disorder

10 February 2025 18:26:00

TABLE II. Peak positions of MoS_2 first-order Raman modes and their FWHMs for 1L MoS_2 and 1L MoS_2 under electron-beam evaporated metals. Starred metals have another peak on the low-frequency side of the $A_1'(\Gamma)^\alpha$ mode.

	$E'(\Gamma)^\alpha$		$A'_1(\Gamma)^\alpha$		Peak intensity (First-order modes)
	Peak position (cm^{-1})	FWHM (cm^{-1})	Peak position (cm^{-1})	FWHM (cm^{-1})	Peak intensity
MoS_2	385.0	4.4	404.5	5.6	High
Cu	384.1	4.0	405.6	4.7	Medium
Pd	384.0	4.1	405.6	5.0	Low
Pt	384.6	4.4	405.1	5.0	Very low
*Bi	383.8	5.5	406.0	4.7	Medium
*Sn	384.4	4.7	405.5	6.0	High
*In	384.6	4.0	404.5	5.9	High

© Author(s) 2024

through theoretical[50] and experimental[6] studies, we do not observe significant peak broadening that could be a signature of structural damage after evaporating the metal films. Peak broadening in the first-order Raman modes of MoS_2 induced by structural damage in the TMD reported in the literature is larger (change in FWHM > 4 cm^{-1})[44,47] than what is measured for our samples.

3. Energy of sputtered atoms and their damage to 1L MoS_2

We expect atoms arriving at the 1L MoS_2 surface with high energy to cause damage, but we are unable to directly measure the energies of the sputtered atoms. However, Spethmann *et al.* determined that for a given angle of incidence of an Ar ion beam, the maximum force a sputtered atom exerts on a surface upon impact increases with decreasing sputter yield.[51] In other words, metals that are easily sputtered require less energy to be released from the target surface and also arrive on the substrate surface with less energy, assuming limited collisions during transport. The sputter yield also tends to increase with the cohesive energy of the target material.[52] We, therefore, compare our Raman spectra of 1L MoS_2 beneath sputtered metals to the cohesive energy of the metals (Fig. 3). Indeed, we observe a correlation between the expected force of sputtered metals of interest (Bi, In, Sn, Cu, Pd, and Pt) and their cohesive energies (taken from).[53] The metals Bi, Sn, Cu with low cohesive energies (2.18, 3.14, and 2.49 eV, respectively) are the same ones with the first-order 1L MoS_2 Raman modes still present after sputtering, with the exception of In (2.52 eV). Interestingly, this correlation also applies to the adsorption energies of the metals on MoS_2, where metals with lower adsorption energies (Bi, Sn, and Cu with adsorption energies of 0.09, 0.63, and =0.77 eV) retained, respectively, the first-order 1L MoS_2 Raman modes, with the exception of In, which has a slightly higher adsorption energy. Hence, it is possible that the disappearance of the 1L MoS_2 peaks beneath In might also be influenced by a slightly higher adsorption energy.

B. Electrical transport properties and characterization

To understand how the electrical properties of the MOCVD-grown MoS_2 films change with PVD technique, a study of Sn/Au contacts for 1L MoS_2 FETs has been conducted. Figure 4(a) shows the FET structure with the MoS_2 channel contacted by 20/30 nm Sn/Au. To create transfer length method (TLM) test structures, we fabricated FETs with 100, 300, 500, and 800 nm channels; a channel width of 4 μm; and a contact length of 1.5 μm on each mesa. Atomic layer deposition (ALD) grown 50 nm Al_2O_3 ($\varepsilon_{ox} \approx 9$) serves as the back-gate dielectric on Pt/TiN/p^{++}-Si substrates. Figures 4(b) and 4(c) show the transfer characteristics, i.e., source-to-drain current (I_D) vs back-gate bias (V_{BG}) for different drain voltages (V_D) for a channel length (L_{CH}) of 100 nm for electron beam evaporated and sputtered contacts, respectively. All the devices exhibited an *n*-type channel, as expected.[54] Figures 4(b) and 4(c) show the ratio of the maximum to minimum current (I_{max}/I_{min}) for the best set of devices for different drain voltages (V_D). Here, I_{max} is the maximum current obtained from the transfer characteristics for $V_D = 1$ V, and I_{min} is the average noise floor. I_{max}/I_{min} was found to be 3×10^7 with evaporated Sn/Au contacts and 4×10^6 with sputtered Sn/Au contact, respectively. The best device had driven currents of $I_{ON} = 58.5\ \mu A/\mu m$ and $I_{ON} = 9.3\ \mu A/\mu m$ with electron-beam evaporated and sputtered Sn/Au contacts, respectively, as shown in Figs. 4(d) and 4(e), while the mean values were 52.25 and 7.76 μA/μm, respectively.

To extract contact resistance (R_C) from the TLM test structure, we used the following equation:

$$R_T = R_{CH} + 2R_C, \tag{1}$$

Here, R_T is the total measured resistance of the FET and R_{CH} is the channel resistance, which is proportional to L_{CH} and inversely proportional to the carrier density (n_s) when the FET is measured in the linear operation regime. We report width-normalized R_C, and we

10 February 2025 18:26:00

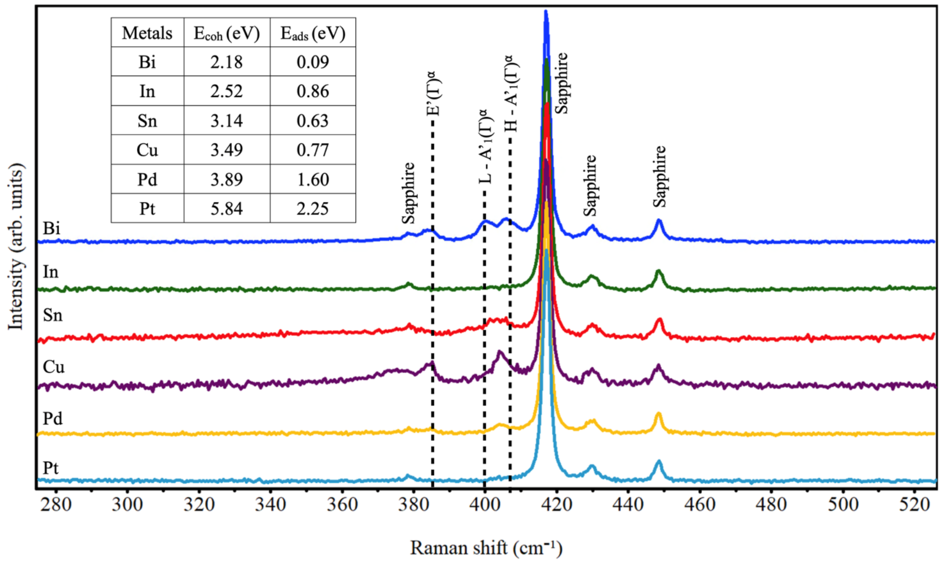

Metals	E_{coh} (eV)	E_{ads} (eV)
Bi	2.18	0.09
In	2.52	0.86
Sn	3.14	0.63
Cu	3.49	0.77
Pd	3.89	1.60
Pt	5.84	2.25

FIG. 3 Summary plot of Raman spectra of sputtered metals on 1L MoS_2 with cohesive and adsorption energies of the metal atoms with respect to the 1L MoS_2 surface.

© Author(s) 2024

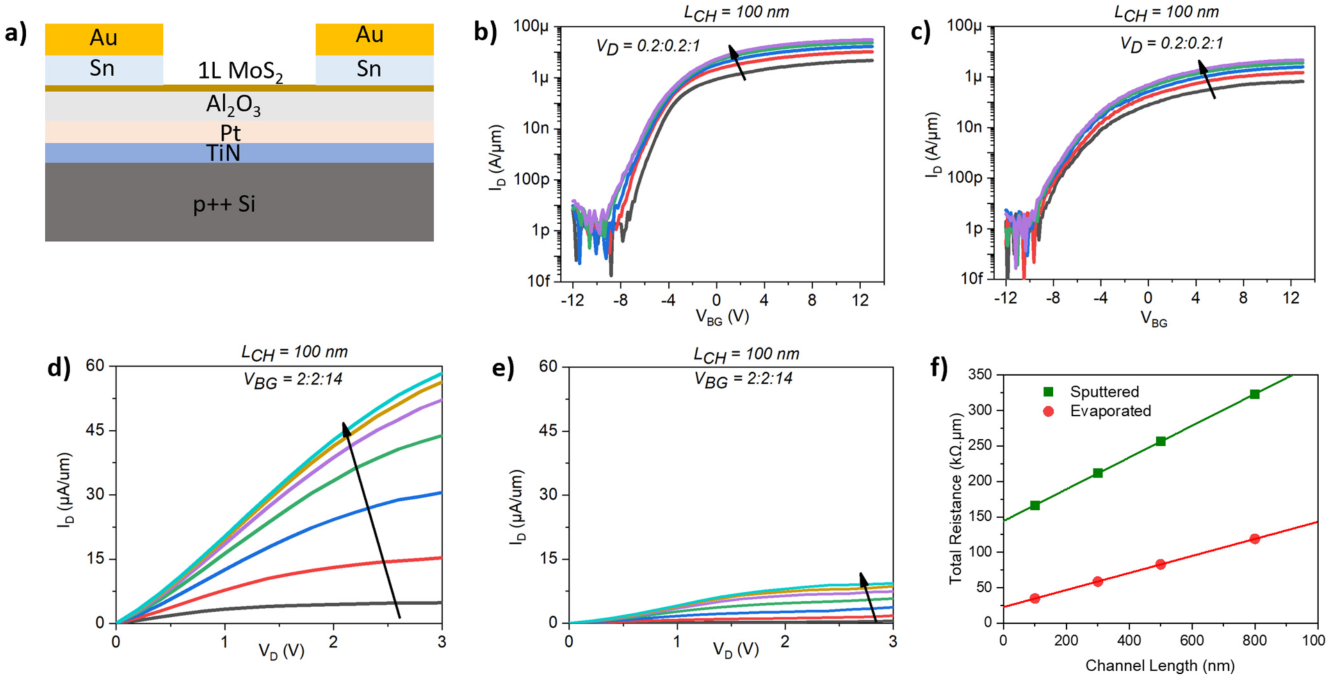

FIG. 4 (a) Schematic of the back-gated FET device structure. (b) and (c) Transfer characteristics, i.e., source-to-drain current (I_D) vs back-gate voltage (V_{BG}) for MoS$_2$ field-effect transistors (FETs) with evaporated and sputtered contacts, respectively. (d) and (e) Output characteristics (I_D–V_D) of the MoS$_2$ FET devices with evaporated and sputtered contacts, respectively. (f) Extracted contact resistance of evaporated and sputtered contacts.

10 February 2025 18:26:00

include four channels with at least one device that is contact resistance-dominated and one that is channel resistance-dominated device.[55] Figure 4(f) shows the extracted contact resistance (R_C) for a carrier concentration (n_s) of $9 \times 10^{12}\ \text{cm}^{-2}$ and $V_D = 1$ V, where we used the following equation to calculate n_s:

$$n_s = \frac{C_{OX}(V_{BG} - V_{TH})}{q}. \tag{2}$$

Here, C_{OX} is the capacitance of the back-gate oxide ($\sim 1.6 \times 10^{-3}\ \text{F m}^{-2}$). The threshold voltage (V_{TH}) was extracted at 10 nA/μm iso-current and showed a slight variation between sputtered and evaporated contacts. Specifically, the mean V_{TH} for sputtered contacts was -4.7 ± 0.8 V, while for electron-beam evaporated contacts, it was -5.3 ± 0.7 V.

Figure 5(a) depicts the distribution of contact resistances of 25 TLM structures with channel lengths of 100, 300, 500, and 800 nm. The best TLM set gave contact resistances of 8.75 and 72 k$\Omega\,\mu$m, while the mean Rc values were 11.25 and 135 k$\Omega\,\mu$m for evaporated and sputtered Sn/Au contacts for $n_S = 9 \times 10^{12}\ \text{cm}^{-2}$, respectively. Hence, sputtered contacts consistently offer higher resistance than evaporated contacts. Interestingly, the slopes of the plots for the

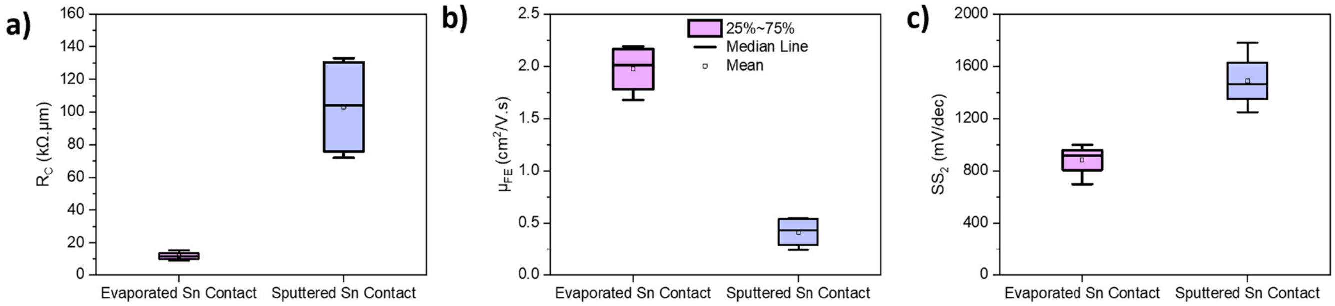

FIG. 5 Statistical analysis with box chart of electrical transport properties of the MoS$_2$ monolayer FET devices: (a) contact resistance, (b) mobility, and (c) subthreshold slope.

© Author(s) 2024

total resistance vs channel width were slightly higher for the sputtered contacts than for the evaporated contacts [Fig. 4(f)], which could reflect an effect on the MoS_2 adjacent to the contacts due to sputtering. For the three-dimensional semiconductor GaN, Molina and Mohney showed that sputtering led to less ideal as-deposited Schottky barrier diodes when rhenium was sputtered compared to when it was electron-beam evaporated.[56] Another study found that process-induced defects in GaN can be introduced well below the metal/semiconductor interface, as detected by deep level transient spectroscopy. Their concentrations depend strongly on metal deposition conditions.[57] We, therefore, suspect that sputter deposition could also have introduced defects in the 2D semiconductor in the adjacent channel of the FETs.

To further compare the performance of the devices, the field-effect mobility (μ_{FE}) and subthreshold slope (*SS*) were determined from 25 FETs having 100 nm channel length. To extract the field-effect mobility (μ_{FE}), the peak transconductance (μ_{gm}) approach was used, as shown in the following equation:

$$\mu_{FE} = g_m \frac{L}{W\ Cox\ VdS};\ g_m = \frac{dI_{DS}}{dV_{BG}}. \tag{3}$$

Here, g_m is the transconductance, W is the channel width, I_D is the drain current, and V_D is the applied drain bias. The subthreshold slope (SS) was calculated as $SS = [d\log(I_D)/dV_{(BG)}]^{-1}$.

The mobility of 2D MoS_2 devices with electron-beam evaporated Sn/Au contact demonstrated superior performance, with a maximum mobility of 2.14 cm^2/V s, a minimum mobility of 1.68 cm^2/V s, and a mean mobility of 2.1 cm^2/V s. In contrast, devices with sputtered contacts exhibited significantly lower mobility values, with a maximum of 0.55 cm^2/V s, a minimum of 0.24 cm^2/V s, and an average mobility of 0.5 cm^2/V s [Fig. 5(b)]. The subthreshold slope (SS) was extracted over two orders of magnitude change in I_D for all MoS_2 FETs with mean values of 880 and 1500 mV/dec for evaporated and sputtered Sn/Au contacts, respectively [Fig. 5(c)].

IV. CONCLUSIONS

This study analyzed the effects of electron-beam evaporated and DC magnetron sputtered metal contacts (Cu, Pd, Bi, Sn, Pt, and In) on 1L MoS_2 using non-destructive backside-illumination Raman spectroscopy. Our results indicated that of the two PVD techniques, the 1L MoS_2 retained its first-order Raman modes after evaporating metal films, although the intensities for Pt were quite low. We were able to observe damage induced in 1L MoS_2 by sputtered metals by the disappearance of the $E'(\Gamma)^\alpha$ and $A'_1(\Gamma)^\alpha$ modes or the significant decrease in their peak intensity, and we found that higher cohesive energies generally correlate with more damage to the semiconductor. Field-effect transistors prepared with evaporated Sn/Au contacts exhibit superior performance metrics compared to FETs with sputtered Sn/Au contacts, including lower contact resistance, enhanced mobility, and improved subthreshold slope compared to their sputtered counterparts. The higher energy of arriving species makes sputter deposition more damaging to monolayer MoS_2 than evaporation of metals, leading to FETs with poorer performance. This work demonstrates the utility of backside Raman spectra, which correlate in an obvious way with device performance, and the approach is recommended for the study of other transition metal dichalcogenide devices.

SUPPLEMENTARY MATERIALS

The supplementary material provides supporting information on (1) evaporation and sputtering conditions, (2) comparison of backside and topside illumination, and (3) the Gaussian–Lorentzian fit to determine the peak positions and full width at half maxima (FWHMs), including the fit for each metal.

ACKNOWLEDGMENTS

The authors acknowledge the primary financial support of the National Science Foundation (NSF) through ECCS 2227346. Epilayers were provided by the Penn State 2D Crystal Consortium—Materials Innovation Platform (2DCC-MIP) under NSF DMR 2039351.

AUTHOR DECLARATIONS

Conflict of Interest

The authors have no conflicts to disclose.

Author Contributions

M. Saifur Rahman: Data curation (equal); Formal analysis (equal); Investigation (equal); Methodology (equal); Writing – original draft (equal). **Ama D. Agyapong:** Data curation (equal); Formal analysis (equal); Investigation (equal); Methodology (equal); Writing – original draft (equal). **Suzanne E. Mohney:** Conceptualization (equal); Investigation (equal); Writing – review & editing (equal).

10 February 2025 18:26:00

DATA AVAILABILITY

The data that support the findings of this study are available from the corresponding author upon reasonable request.

REFERENCES

[1] A. Nourbakhsh, A. Zubair, R. N. Sajjad, A. K. G. Tavakkoli, W. Chen, S. Fang, X. Ling, J. Kong, M. S. Dresselhaus, E. Kaxiras, K. K. Berggren, D. Antoniadis, and T. Palacios, "MoS_2 field-effect transistor with sub-10 nm channel length," Nano Lett. **16**(12), 7798–7806 (2016).

[2] A. Sebastian, R. Pendurthi, T. H. Choudhury, J. M. Redwing, and S. Das, "Benchmarking monolayer MoS_2 and WS_2 field-effect transistors," Nat. Commun. **12**(1), 693 (2021).

[3] M. Chhowalla, D. Jena, and H. Zhang, "Two-dimensional semiconductors for transistors," Nat. Rev. Mater. **1**(11), 1–15 (2016).

[4] Y. Wang, J. C. Kim, R. J. Wu, J. Martinez, X. Song, J. Yang, F. Zhao, A. Mkhoyan, H. Y. Jeong, and M. Chhowalla, "Van der Waals contacts between three-dimensional metals and two-dimensional semiconductors," Nature **568**(7750), 70–74 (2019).

[5] B. Radisavljevic, A. Radenovic, J. Brivio, V. Giacometti, and A. Kis, "Single-layer MoS_2 transistors," Nat. Nanotechnol. **6**(3), 147–150 (2011).

[6] K. Schauble, D. Zakhidov, E. Yalon, S. Deshmukh, R. W. Grady, K. A. Cooley, C. J. McClellan, S. Vaziri, D. Passarello, S. E. Mohney, M. F. Toney, A. K. Sood, A. Salleo, and E. Pop, "Uncovering the effects of metal contacts on monolayer MoS_2," ACS Nano **14**(11), 14798–14808 (2020).

[7] Y. Wang and M. Chhowalla, "Making clean electrical contacts on 2D transition metal dichalcogenides," Nat. Rev. Phys. **4**(2), 101–112 (2022).

© Author(s) 2024

[8] Y. Liu, J. Guo, E. Zhu, L. Liao, S.-J. Lee, M. Ding, I. Shakir, V. Gambin, Y. Huang, and X. Duan, "Approaching the Schottky–Mott limit in van der Waals metal–semiconductor junctions," Nature **557**(7707), 696–700 (2018).

[9] Y. Jung, M. S. Choi, A. Nipane, A. Borah, B. Kim, A. Zangiabadi, T. Taniguchi, K. Watanabe, W. J. Yoo, J. Hone, and J. T. Teherani, "Transferred via contacts as a platform for ideal two-dimensional transistors," Nat. Electron. **2**(5), 187–194 (2019).

[10] B. Ayachi, T. Aviles, J.-P. Vilcot, C. Sion, and P. Miska, "Room temperature pulsed-DC sputtering deposition process for CIGS absorber layer: Material and device characterizations," Thin Solid Films **660**, 175–179 (2018).

[11] R. Garg, S. Gonuguntla, S. Sk, M. S. Iqbal, A. O. Dada, U. Pal, and M. Ahmadipour, "Sputtering thin films: Materials, applications, challenges and future directions," Adv. Colloid Interface Sci. **330**, 103203 (2024).

[12] A.-S. Chou, Y.-T. Lin, Y. C. Lin, C.-H. Hsu, M.-Y. Li, S.-L. Liew, S.-A. Chou, H.-Y. Chen, H.-Y. Chiu, P.-H. Ho, M.-C. Hsu, Y.-W. Hsu, N. Yang, W.-Y. Woon, S. Liao, D.-H. Hou, C.-H. Chien, W.-H. Chang, I. Radu, C.-I. Wu, H.-S. Philip Wong, and H. Wang, "High-performance monolayer WSe$_2$ p/n FETs via antimony-platinum modulated contact technology towards 2D CMOS electronics," in *2022 International Electron Devices Meeting (IEDM)* (IEEE, 2022), pp. 7.2.1–7.2.4.

[13] R. Nakajima, T. Nishimura, K. Ueno, and K. Nagashio, "Work function modulation of Bi/Au bilayer system toward p-type WSe$_2$ FET," ACS Appl. Electron. Mater. **6**(1), 144–149 (2024).

[14] S. Ghods, H. Lee, J.-H. Choi, J.-Y. Moon, S. Kim, S.-I. Kim, H. J. Kwun, M. J. Josline, C. Y. Kim, S. H. Hyun, S. W. Kim, S.-K. Son, T. Lee, Y. K. Lee, K. Heo, K. S. Novoselov, and J.-H. Lee, "Topological van der Waals contact for two-dimensional semiconductors," ACS Nano **18**(38), 26192–26200 (2024).

[15] A. Seredinski, e.g., Arnault, V. Z. Costa, L. Zhao, T. F. Q. Larson, K. Watanabe, T. Taniguchi, F. Amet, A. K. M. Newaz, and G. Finkelstein, "One-dimensional edge contact to encapsulated MoS$_2$ with a superconductor," AIP Adv. **11**(4), 045312 (2021).

[16] R.-S. Chen, G. Ding, Y. Zhou, and S.-T. Han, "Fermi-level depinning of 2D transition metal dichalcogenide transistors," J. Mater. Chem. C Mater. **9**(35), 11407–11427 (2021).

[17] X. Liu, M. S. Choi, E. Hwang, W. J. Yoo, and J. Sun, "Fermi level pinning dependent 2D semiconductor devices: Challenges and prospects," Adv. Mater. **34**(15), 2108425 (2022).

[18] M. Ohring, "Thin-Film evaporation processes," in *Materials Science of Thin Films* (Elsevier, 2002), pp. 95–144.

[19] W. H. Chang, S. Hatayama, Y. Saito, N. Okada, T. Endo, Y. Miyata, and T. Irisawa, "Sb$_2$Te$_3$/MoS$_2$ van der Waals junctions with high thermal stability and low contact resistance," Adv. Electron. Mater. **9**(4), 2201091 (2023).

[20] Y. Wang, J. C. Kim, Y. Li, K. Y. Ma, S. Hong, M. Kim, H. S. Shin, H. Y. Jeong, and M. Chhowalla, "P-type electrical contacts for 2D transition-metal dichalcogenides," Nature **610**(7930), 61–66 (2022).

[21] Y. Huang, Y. Gu, S. Mohan, A. Dolocan, N. D. Ignacio, S. Kutagulla, K. Matthews, A. Londoño-Calderon, Y. Chang, Y. Chen, J. H. Warner, M. T. Pettes, J. C. Lee, and D. Akinwande, "Reliability improvement and effective switching layer model of thin-film MoS$_2$ memristors," Adv. Funct. Mater. **34**(15), 2214250 (2024).

[22] X. Wang, Y. Hu, S. Y. Kim, R. Addou, K. Cho, and R. M. Wallace, "Origins of Fermi level pinning for Ni and Ag metal contacts on tungsten dichalcogenides," ACS Nano **17**(20), 20353–20365 (2023).

[23] C. D. English, G. Shine, V. E. Dorgan, K. C. Saraswat, and E. Pop, "Improved contacts to MoS$_2$ transistors by ultra-high vacuum metal deposition," Nano Lett. **16**(6), 3824–3830 (2016).

[24] W. Zheng, B. Yuan, M. A. Villena, K. Zhu, S. Pazos, Y. Shen, Y. Yuan, Y. Ping, C. Liu, X. Zhang, X. Zhang, and M. Lanza, "The origin and mitigation of defects induced by metal evaporation in 2D materials," Mater. Sci. Eng., R **160**, 100831 (2024).

[25] Z. Sun, S. Y. Kim, J. Cai, J. Shen, H.-Y. Lan, Y. Tan, X. Wang, C. Shen, H. Wang, Z. Chen, R. M. Wallace, and J. Appenzeller, "Low contact resistance on monolayer MoS$_2$ field-effect transistors achieved by CMOS-compatible metal contacts," ACS Nano **18**(33), 22444–22453 (2024).

[26] S. McDonnell, C. Smyth, C. L. Hinkle, and R. M. Wallace, "MoS$_2$—Titanium contact interface reactions," ACS Appl. Mater. Interfaces **8**(12), 8289–8294 (2016).

[27] C. Gong, C. Huang, J. Miller, L. Cheng, Y. Hao, D. Cobden, J. Kim, R. S. Ruoff, R. M. Wallace, K. Cho, X. Xu, and Y. J. Chabal, "Metal contacts on physical vapor deposited monolayer MoS$_2$," ACS Nano **7**(12), 11350–11357 (2013).

[28] A. D. Agyapong, K. A. Cooley, and S. E. Mohney, "Reactivity of contact metals on monolayer WS$_2$," J. Appl. Phys. **128**(5), 055306 (2020).

[29] P.-C. Shen, C. Su, Y. Lin, A.-S. Chou, C.-C. Cheng, J.-H. Park, M.-H. Chiu, A.-Y. Lu, H.-L. Tang, M. M. Tavakoli, G. Pitner, X. Ji, Z. Cai, N. Mao, J. Wang, V. Tung, J. Li, J. Bokor, A. Zettl, C.-I. Wu, T. Palacios, L.-J. Li, and J. Kong, "Ultralow contact resistance between semimetal and monolayer semiconductors," Nature **593**(7858), 211–217 (2021).

[30] A. Kumar, K. Schauble, K. M. Neilson, A. Tang, P. Ramesh, H.-S. P. Wong, E. Pop, and K. Saraswat, "Sub-200 $\Omega \cdot \mu$m alloyed contacts to synthetic monolayer MoS$_2$," in *2021 IEEE International Electron Devices Meeting (IEDM)* (IEEE, 2021), pp. 7.3.1–7.3.4.

[31] C. Chen, N. Trainor, S. Kumari, H. Myja, T. Kümmell, Z. Zhang, Y. Zhang, A. Bisht, M. U. K. Sadaf, N. U. Sakib, Y. Han, T. V. Mc Knight, A. R. Graves, M. E. Leger, N. D. Redwing, M. Kim, D. A. Kowalczyk, G. Bacher, N. Alem, Y. Yang, S. Das, and J. M. Redwing, "Effect of growth temperature on the microstructure and properties of epitaxial MoS$_2$ monolayers grown by metalorganic chemical vapor deposition," J. Vac. Sci. Technol. A **42**(2), 022201 (2024).

[32] Y. Xiang, X. Sun, L. Valdman, F. Zhang, T. H. Choudhury, M. Chubarov, J. A. Robinson, J. M. Redwing, M. Terrones, Y. Ma, L. Gao, M. A. Washington, T.-M. Lu, and G.-C. Wang, "Monolayer MoS$_2$ on sapphire: An azimuthal reflection high-energy electron diffraction perspective," 2D Mater. **8**(2), 025003 (2021).

[33] A. Mazzoni, R. Burke, M. Chin, S. Najmaei, M. Dubey, N. Goldsman, and K. Daniels, "Comparison of contact metals evaporated onto monolayer molybdenum disulfide," J. Appl. Phys. **132**, 224305 (2022).

[34] N. Kaushik, A. Nipane, F. Basheer, S. Dubey, S. Grover, M. M. Deshmukh, and S. Lodha, "Schottky barrier heights for Au and Pd contacts to MoS$_2$," Appl. Phys. Lett. **105**(11), 113505 (2014).

[35] Z. Cao, F. Lin, G. Gong, H. Chen, and J. Martin, "Low Schottky barrier contacts to 2H-MoS$_2$ by Sn electrodes," Appl. Phys. Lett. **116**(2), 022101 (2020).

[36] X. Zhang, X.-F. Qiao, W. Shi, J.-B. Wu, D.-S. Jiang, and P.-H. Tan, "Phonon and Raman scattering of two-dimensional transition metal dichalcogenides from monolayer, multilayer to bulk material," Chem. Soc. Rev. **44**(9), 2757–2785 (2015).

[37] B. Chakraborty, A. Bera, D. V. S. Muthu, S. Bhowmick, U. V. Waghmare, and A. K. Sood, "Symmetry-dependent phonon renormalization in monolayer MoS$_2$ transistor," Phys. Rev. B **85**(16), 161403 (2012).

[38] F. Zhang, C. Erb, L. Runkle, X. Zhang, and N. Alem, "Etchant-free transfer of 2D nanostructures," Nanotechnology **29**(2), 025602 (2018).

[39] E. Mercado, A. Goodyear, J. Moffat, M. Cooke, and R. S. Sundaram, "A Raman metrology approach to quality control of 2D MoS$_2$ film fabrication," J. Phys. D: Appl. Phys. **50**(18), 184005 (2017).

[40] J. M. Chen and C. S. Wang, "Second order Raman spectrum of MoS$_2$," Solid State Commun. **14**(9), 857–860 (1974).

[41] M. Kadleíková, J. Breza, and M. Veselý, "Raman spectra of synthetic sapphire," Microelectron. J. **32**(12), 955–958 (2001).

[42] P. Kumar and R. Nagarajan, "An elegant room temperature procedure for the precise control of composition in the Cu–S system," Inorg. Chem. **50**(19), 9204–9206 (2011).

[43] M. A. Bissett, M. Tsuji, and H. Ago, "Strain engineering the properties of graphene and other two-dimensional crystals," Phys. Chem. Chem. Phys. **16**(23), 11124–11138 (2014).

[44] M. W. Iqbal, K. Shahzad, R. Akbar, and G. Hussain, "A review on Raman finger prints of doping and strain effect in TMDCs," Microelectron. Eng. **219**, 111152 (2020).

10 February 2025 18:26:00

[45]K. P. Dhakal, D. L. Duong, J. Lee, H. Nam, M. Kim, M. Kan, Y. H. Lee, and J. Kim, "Confocal absorption spectral imaging of MoS_2: Optical transitions depending on the atomic thickness of intrinsic and chemically doped MoS_2," Nanoscale **6**(21), 13028–13035 (2014).

[46]S. Zhang, H. M. Hill, K. Moudgil, C. A. Richter, A. R. Hight Walker, S. Barlow, S. R. Marder, C. A. Hacker, and S. J. Pookpanratana, "Controllable, wide-ranging n-doping and p-doping of monolayer group 6 transition-metal disulfides and diselenides," Adv. Mater. **30**(36), 1802991 (2018).

[47]G. L. Frey, R. Tenne, M. J. Matthews, M. S. Dresselhaus, and G. Dresselhaus, "Raman and resonance Raman investigation of MoS_2 nanoparticles," Phys. Rev. B **60**(4), 2883–2892 (1999).

[48]W. Zhao, Q. Wu, Q. Hao, J. Wang, M. Li, Y. Zhang, K. Bi, Y. Chen, and Z. Ni, "Plasmon–phonon coupling in monolayer WS_2," Appl. Phys. Lett. **108**(13), 131903 (2016).

[49]T. Feng, D. Wang, C. Wang, N. Chen, H. Hahn, and H. Gleiter, "Generating metallic amorphous core–shell nanoparticles by a solid-state amorphization process," Part. Part. Syst. Charact. **33**(2), 82–88 (2016).

[50]S. Mignuzzi, A. J. Pollard, N. Bonini, B. Brennan, I. S. Gilmore, M. A. Pimenta, D. Richards, and D. Roy, "Effect of disorder on Raman scattering of single-layer MoS_2," Phys. Rev. B **91**(19), 195411 (2015).

[51]A. Spethmann, T. Trottenberg, and H. Kersten, "Measurement and simulation of the momentum transferred to a surface by deposition of sputtered atoms*," Eur. Phys. J. D **70**(12), 255 (2016).

[52]M. P. Seah, "Universal equation for argon gas cluster sputtering yields," J. Phys. Chem. C **117**(24), 12622–12632 (2013).

[53]W. A. Saidi, "Trends in the adsorption and growth morphology of metals on the MoS_2 (001) surface," Cryst. Growth Des. **15**(7), 3190–3200 (2015).

[54]S. Das, H. Y. Chen, A. V. Penumatcha, and J. Appenzeller, "High performance multilayer MoS_2 transistors with scandium contacts," Nano Lett. **13**(1), 100–105 (2013).

[55]Z. Cheng, C.-S. Pang, P. Wang, S. T. Le, Y. Wu, D. Shahrjerdi, I. Radu, M. C. Lemme, L.-M. Peng, X. Duan, Z. Chen, J. Appenzeller, S. J. Koester, E. Pop, A. D. Franklin, and C. A. Richter, "How to report and benchmark emerging field-effect transistors," Nat. Electron. **5**(7), 416–423 (2022).

[56]A. Molina and S. E. Mohney, "Improved rhenium Schottky diodes to n-type gallium nitride," Mater. Sci. Semicond. Process. **148**, 106799 (2022).

[57]F. D. Auret, S. A. Goodman, G. Myburg, S. E. Mohney, and J. M. de Lucca, "Processing-induced electron traps in n-type GaN," Mater. Sci. Eng. B **82**(1–3), 102–104 (2001).

10 February 2025 18:26:00

© Author(s) 2024